JOURNAL OF MATERIALS SCIENCE **39** (2004) 4869–4875

Dynamic behavior of SUS304 stainless steel at elevated temperatures

XIAOHONG CHEN, YANG WANG, MING GONG, YUANMING XIA*
Department of Mechanics and Mechanical Engineering, Key Laboratory of Mechanical Behavior and Design of Materials, University of Science and Technology of China, CAS, Hefei, Anhui 230027, People's Republic of China
E-mail: ymxia@ustc.edu.cn

An elevated temperature tensile impact experimental technique has been developed, using the rotating disk indirect bar-bar tensile impact apparatus with elevated temperature furnaces. Temperatures up to 800°C in the specimen have been obtained by means of rapid contact heating.

Tensile impact experiments have been performed to investigate the mechanical behavior of SUS304 stainless steel in the temperature range 25–537°C. In contrast, the quasi-static tensions were conducted on MTS810 at three temperatures 25, 400 and 537°C, respectively. The experimental results show that the elevated temperature tensile impact experimental technique and method adopted are feasible practically. SUS304 stainless steel is a sort of temperature and strain-rate dependent metal, i.e., the strain rate has the effect of strengthening on yield stress and ultimate stress, but embrittling on unstable strain. The unstable strain decreases with increasing temperature at a constant strain rate, exhibiting an elevated temperature embrittlement phenomenon. The microstructure analysis reveals that the elevated temperature embrittlement phenomenon is due to the 'sensitization' of SUS304. In the case of impact loading, the adiabatic temperature rise is also capable of leading to sensitization. The differences of specimens' fractograph between tensile impact and quasi-static tension probably involve different deformation and fracture mechanisms. It is found that the volume fraction of $\gamma \rightarrow \alpha'$ transformation is strain, temperature and strain-rate dependent. © *2004 Kluwer Academic Publishers*

1. Introduction

The modern Split-Hopkinson pressure bar technique (SHPB), first developed by Kolsky in 1949 [1], has been widely applied to study the dynamic properties of solid materials. Recently, with the developments of the technique [2, 3], dynamic compression tests at elevated temperatures have been conducted on SHPB in a few labs [4, 5]. Harding designed a block-bar spilt-Hopkinson tensile bar apparatus (SHTB) in 1960 [6], and developed a direct bar-bar SHTB apparatus in 1982. Much good effort was paid in this field by them [7, 8]. Kawata [9], Nicholas [10], Staab and Gilat [11] independently developed a different dynamic tensile technique, respectively. Xia designed a rotating disk indirect bar-bar tensile impact apparatus in 1988. Tensile impact experiments for kinds of metallic and nonmetallic materials were performed on this apparatus and a lot of interesting results were brought out in the recent decade [12–20]. In the field of tensile impact tests at elevated temperatures, D. C. Barton denoted a technique based on the induction heating process to rapidly heat metallic specimens prior to high strain rate testing on a 'Flying Wedge' tensile testing machine, producing temperatures up to 600°C and a strain rate $>10^3$ s^{-1} [21]. An empirical fracture model for pure iron was dealt with, and no completed stress/time, strain/time or strain rate/time curves were presented in Ref. [21]. This paper aims to develop an elevated temperature tensile impact technique up to 800°C, and to investigate the dynamic mechanical behavior of stainless steel SUS304 at elevated temperatures, and to explore the mechanism of the mechanical properties dependence of temperature and strain-rate for SUS304 stainless steel through an analysis of microstructure of the specimen fractures.

2. Experiment

2.1. Elevated temperature tensile tests

Elevated temperature tensile tests both with quasi-static and high strain-rate loading were involved in the present work. The quasi-static experiments were performed on a MTS810 material testing machine at a strain rate of 0.001 s^{-1} with three different environment temperatures 25, 400 and 537°C, respectively. The tensile impact experiments were performed on the

*Author to whom all correspondence should be addressed.

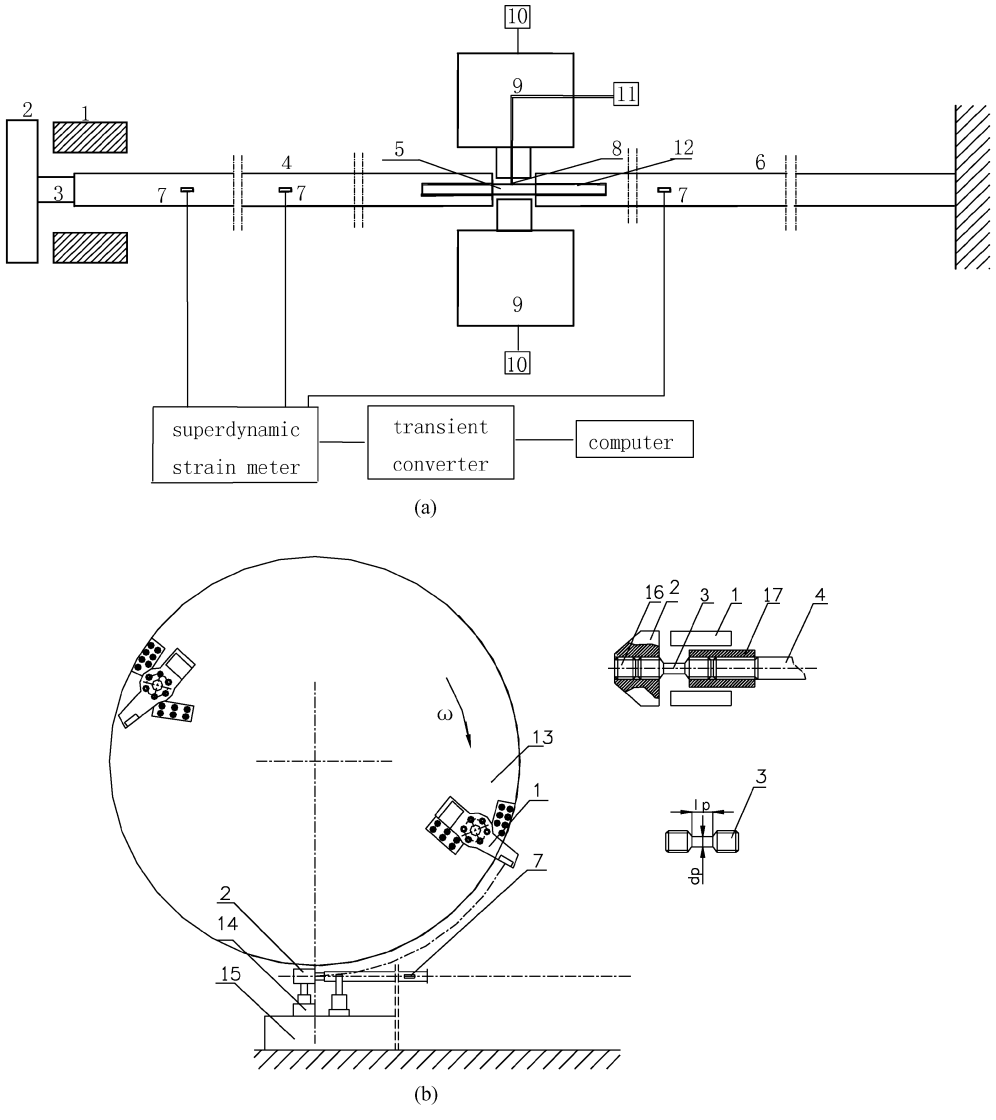

Figure 1 Schematic diagram of tensile impact apparatus. 1. impact hammer 2. impact block 3. short prefixed metal bar 4. incident bar 5. specimen 6. transmitted bar 7. strain gauge 8. thermocouple 9. elevated temperature furnace 10. thermoregulator of furnaces 11. temperature measurement system of specimen 12. adhesive layer 13. disk 14. impact block support 15. rigid base 16. puller bolt 17. connector.

self-designed rotating disk indirect bar-bar tensile impact apparatus at a strain rate of 1200 s^{-1} with three environment different temperatures 25, 250 and 537°C, respectively.

The indirect bar-bar tensile impact apparatus consists of a rotating disk loading system, an impact block, a pre-fixed metal bar, an incident bar, a transmitted bar and a data acquisition system. Scheme of the bar-bar tensile impact apparatus is shown in Fig. 1a and b. When the rotating disk (13) reaches the required rotating speed, the impact hammer (1), fixed on the rotating disk, protrudes and strikes the impact block (2). The short pre-fixed metal bar (3) between the block and the incident bar (4) is broken away so that an approximately rectangular stress pulse is produced in the incident bar. Partial of the incident pulse is transmitted through the specimen (5) to the transmitted bar (6) and the residual is reflected to the incident bar. By adjusting the impact speed of the rotating disk as well as the diameter or length of the short metal bar, different amplitude, width and rise time of tensile impulses are available for any particular tests at a certain strain rate. The strain signals of the incident wave $\varepsilon_i(t)$, reflected wave $\varepsilon_r(t)$ and transmitted wave $\varepsilon_t(t)$ are picked up from the strain gauges (7) on the incident/transmitted bars by the superdynamic strain meter, respectively. The strain gauges used in the tests are semiconductor strain gauges with a size of 3 mm. The response frequencies of a self-designed type KGS-II superdynamic strain meter (amplifier) are 10 Hz–2 MHz. The signals are recorded by a TCL transient converter with a sampling rate of 20 MHz.

According to the one-dimensional simple-wave theory, the strain $\varepsilon_s(t)$, strain-rate $\dot{\varepsilon}_s(t)$ and stress $\sigma_s(t)$ in the specimen can be written as follows:

$$\varepsilon_s(t) = \frac{2C}{l_0}\int_0^t [\varepsilon_i(\tau) - \varepsilon_t(\tau)]\,d\tau \tag{1}$$

$$\dot{\varepsilon}_s(t) = \frac{2C}{l_0}[\varepsilon_i(t) - \varepsilon_t(t)] \tag{2}$$

$$\sigma_s(t) = \frac{EA}{A_s}\varepsilon_t(t) \tag{3}$$

where E, A and C are the Young's modulus, cross-sectional area and elastic wave velocity of the

incident/transmitted bars, respectively. l_0 and A_s are the length and the cross-sectional area of the testing gauge of the specimen, respectively.

2.2. Specimen geometry and connection

The material used in this work was SUS304 austenitic stainless steel with the chemical composition: 18.52Cr-8.34Ni-0.89Mn-0.42Si-0.002P-0.002S-0.046C in weight percent and the balance Fe. The specimens, with dumbbell-shaped flat, 1.1 mm thickness, are illustrated in Figs 2 and 3 for quasi-static and tensile impact, respectively. A refractory inorganic adhesive was used to connect dynamic specimen with incident/transmitted bars, as shown in Fig. 4. The thickness of each adhesive layer was 0.10 mm. The geometry of the dynamic specimen used at elevated temperatures in the present work was approximately the same as the R. T. specimen used before [15–17]. The thickness of adhesive layer was increased to 0.10 mm in view of the difference between inorganic adhesive and organic adhesive. The geometry of the specimens and the thickness of adhesive layer (0.05 mm) in Ref. [15–17] were determined by way of experimental methods [22, 23] and numerical analysis cooperated with experiments [24, 25], in which the influence of temperature was not dealt with. The validity of the geometry of specimens and the thickness of adhesive layers in elevated temperature tests in the present work needs to be further evidenced.

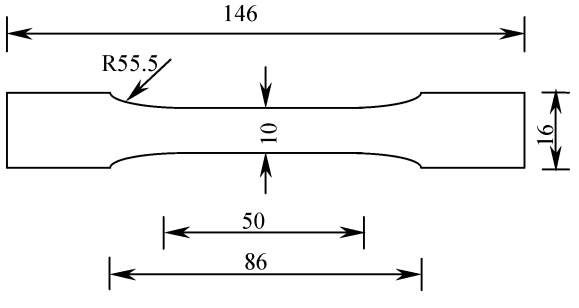

Figure 2 Specimen geometry for quasi-static tests.

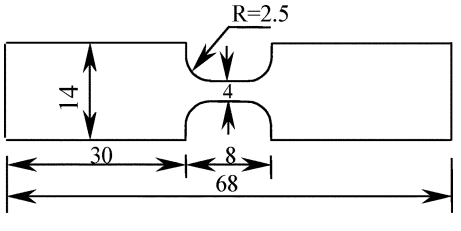

Figure 3 Specimen geometry for tensile impact tests.

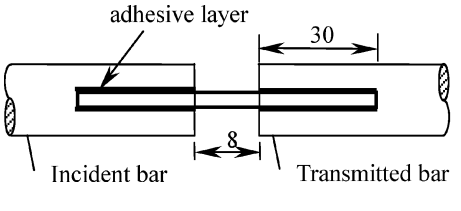

Figure 4 Connection of specimen to bars.

2.3. Rapid contact heating and elevated temperature tests

The specimen was stuck to the slots of the incident/transmitted bars with the refractory inorganic adhesive. Two furnaces with metal-core axes were located at both sides apart from the specimen. The furnaces were first turned on. Temperature kept rising until the temperature reached the set point and remained stable, as shown in Fig. 5a, then the furnaces were moved to make each end of metal-core axes touch either surface of the specimen simultaneously, as shown in Fig. 5b. After 1–2 min heated, once an approximate even temperature field of the testing region of the specimen was achieved, the tensile impact experiments were performed. Several WRP-100 Pt-Rh thermocouples were used to measure the temperature. The experimental results indicate that a temperature up to 800°C in the specimen can be obtained using this rapid contact heating system.

2.4. Microstructure examination

The microstructure of specimens on each testing conditions were analyzed. The surface analysis of fracture was carried out on an XL-30 Environmental Scanning Electron Microscope (ESEM). The volume of $\gamma \rightarrow \alpha'$ transformation was detected on a type of X-350A X-ray Diffraction Meter (XRD). At last the broken specimens were cut along the tensile direction and ground as metallographic samples. The microstructures were inspected on an XJG-05 Metallurgical Microscope.

3. Results and analysis

3.1. Tensile experimental results

A typical wave forms at 537°C and a strain rate of 1200 s^{-1} is shown in Fig. 6. The strain/time, stress/time, strain rate/time curves in the corresponding testing are shown in Fig. 7. The complete stress/strain curves for the SUS304 stainless steel at two strain rates and various temperatures are shown in Figs 8 and 9, respectively. The correlation between $\sigma_{0.2}$, σ_b, ε_b and temperature are shown in Fig. 10. The yield stress $\sigma_{0.2}$, ultimate stress σ_b, unstable strain ε_b (corresponding to σ_b) and their deviations at quasi-static and tensile impact tests are listed in Tables I and II, respectively.

From Tables I and II and Figs 8–10, it can be observed that

(1) Not only $\sigma_{0.2}$ and σ_b of SUS304 but also ε_b decreases with increasing temperature under both quasi-static and tensile impact loading conditions. There is an obvious elevated temperature embrittlement phenomenon for SUS304 stainless steel.

(2) At temperatures 25 and 537°C, $\sigma_{0.2}$ and σ_b at a strain rate of 1200 s^{-1} are greater than those at rate of 0.001 s^{-1}. However, ε_b decreases at a strain rate of 1200 s^{-1} compared with the quasi-static data. It shows that the strain rate has the effect of strengthening yield stress and ultimate stress, but embrittling on unstable strain.

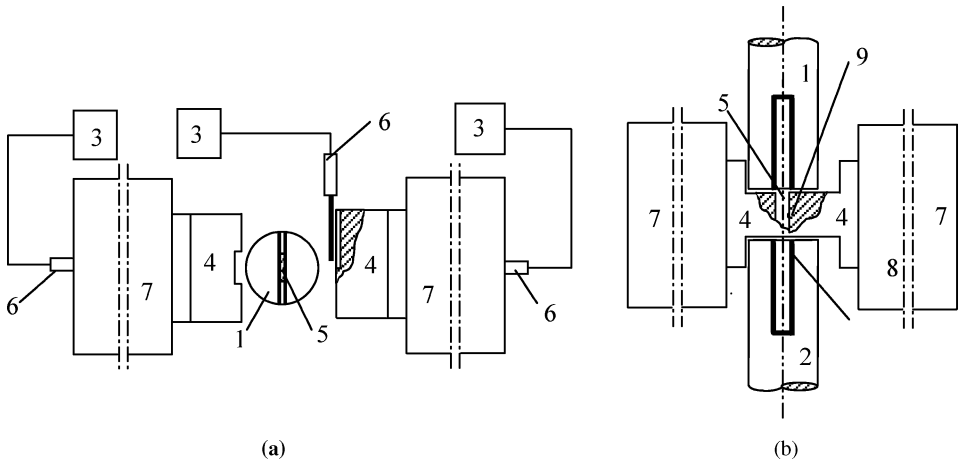

Figure 5 Schematic diagrams of contact heating. (a) Heating the furnaces (b) Contacting to heat the specimen 1. incident bar 2. transmitted bar 3. thermoregulator 4. metal-core axes 5. specimen 6. thermocouple 7. elevated temperature furnace 8. adhesive layer 9. thermocouple wires.

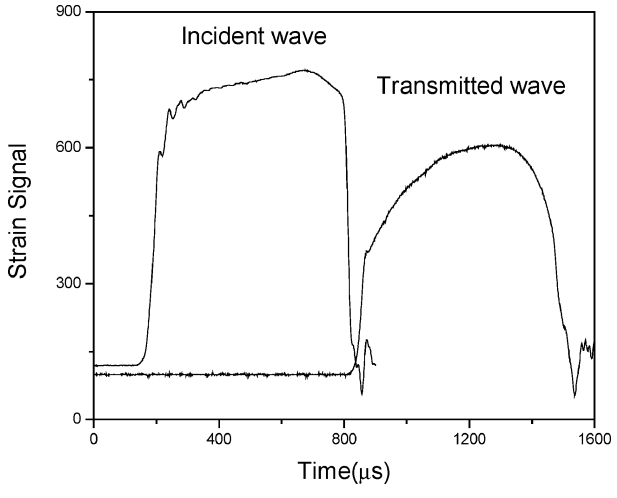

Figure 6 A typical record of wave forms ($\dot{\varepsilon} = 1200\ s^{-1}$, 537°C).

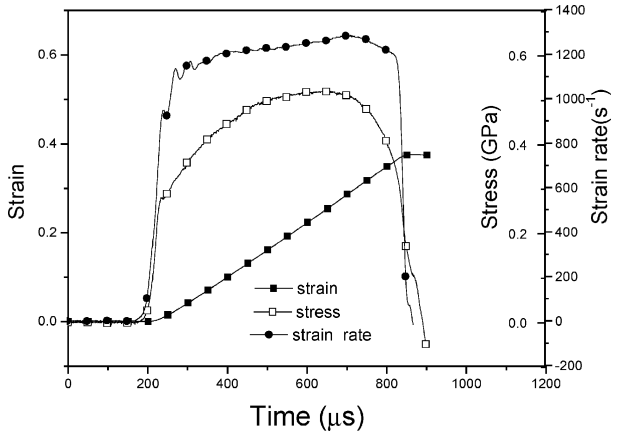

Figure 7 Stress/time, strain/time and strain rate/time curves of SUS304 at 537°C and an average strain rate of 1200 s^{-1}.

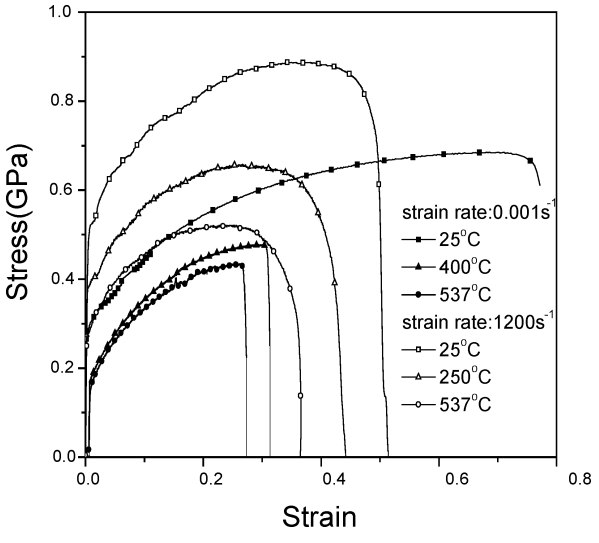

Figure 8 Stress/strain curves of SUS304 at different temperatures ($\dot{\varepsilon} = 0.001\ s^{-1}$ and $\dot{\varepsilon} = 1200\ s^{-1}$).

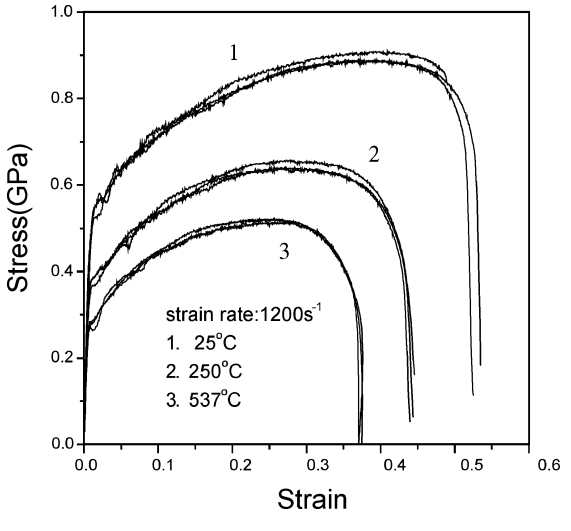

Figure 9 Stress/strain curves of SUS304 at different temperatures ($\dot{\varepsilon} = 1200\ s^{-1}$).

3.2. Microstructure examination results and analysis

The microstructure analysis shows that carbides are deposited in the matrix at 400 and 537°C in quasi-static specimens, but no carbides are found at 25°C. Furthermore, the sizes and quantities of carbides increase with increasing temperature. Such results agree with that in Ref. [26], which indicates that sensitization exists in austenite stainless steel. It may be the reason that the elevated temperature embrittlement phenomenon emerges in quasi-static tension. The only difference is that the sensitization temperature shown in the present paper is lower than that in Ref. [26]. In specimens impacted at 250 and 537°C, it can be observed that

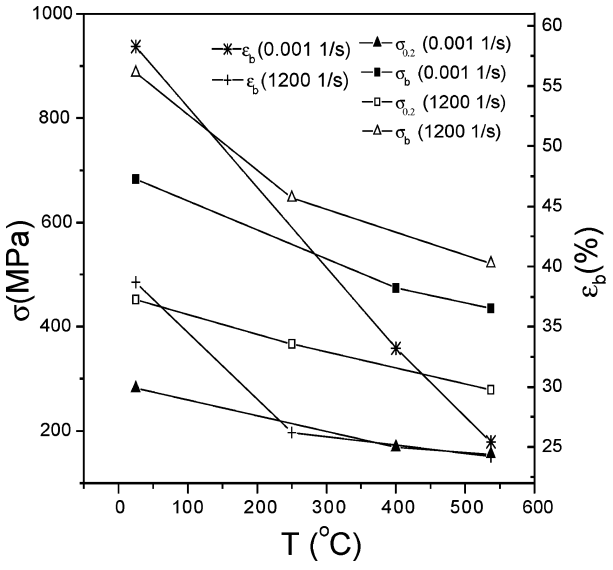

Figure 10 $\sigma_{0.2}$, ε_b and σ_b vs. T (Temperature).

TABLE I Mechanical properties of SUS304 stainless steel at different temperatures ($\dot{\varepsilon} = 0.001\ s^{-1}$)

Temperature (°C)	$\sigma_{0.2}$ (MPa)	σ_b (MPa)	ε_b (%)
Room (25)	452 ± 2.9	887 ± 2.2	38.68 ± 0.79
250	367 ± 5.8	647 ± 4.4	26.20 ± 1.09
537	279 ± 4.4	521 ± 5.2	24.20 ± 1.07

TABLE II Mechanical properties of SUS304 stainless steel at different temperatures ($\dot{\varepsilon} = 1200\ s^{-1}$)

Temperature (°C)	Initial modulus E (GPa)	$\sigma_{0.2}$ (MPa)	σ_b (MPa)	ε_b (%)
Room (25)	210 ± 3.2	282 ± 1.6	683 ± 3.1	58.3 ± 0.28
400	169 ± 4.2	169 ± 6.8	474 ± 4.0	29.5 ± 0.50
537	165 ± 3.2	155 ± 2.6	435 ± 2.0	25.4 ± 0.80

the way of precipitation of carbides is similar to that in quasi-static specimens. This indicates that the elevated temperature embrittlement phenomenon at high strain rate may be also caused by sensitization. The microstructure of the tensile impact specimen tested at 537°C is shown in Fig. 11b. Moreover, it is interesting to see that precipitation of carbides also are found in the tensile impact specimen at 25°C as shown in Fig. 11a. Tensile impact approaches an adiabatic process, and results in the adiabatic temperature rise [27–29] might exceed the sensitization temperature of SUS304 during that process. More research is needed to investigate the mechanism of the precipitation of carbides in the tensile impact specimen at 25°C.

The quasi-static fractographs (SEM) of SUS304 specimens at 25 and 400°C are shown in Fig. 12. Although shear lip by dislocation slip can be obviously seen in both, the microstructures are markedly different in the central parts. Even uniaxial dimples and a few microbores can be seen in the specimen at 25°C. No precipitations are found at the bottom of microbores as shown in Fig. 12a, which presents a typical ductile fracture characteristic. For the specimen at 400°C, a mixed pattern with uneven dimples and quasi-cleavage are observed with some precipitations at the bottom of microbores. A few macroscopic-voids are clearly seen as shown in Fig. 12b, which exhibits a characteristic of brittle fracture. The microstructure of the quasi-static tensile specimens at 537°C is similar to that at 400°C. It is consistent with the elevated temperature embrittlement phenomenon caused by the sensitization.

The tensile impact fractograph (SEM) of SUS304 specimens at 25°C is shown in Fig. 13. Compared with the quasi-static specimens, the fracture surface looks smoother without distinct shear lip. The fractograph shows a typical dimple pattern, with egg-shaped scattering near the edge of the surface as shown in Fig. 13a and even uniaxial in the central part. A few microbores accompanied with the precipitation of secondary phases can be found apparently as shown in Fig. 13b. The tensile fracture surfaces at 250 and 537°C are similar to those at 25°C. The precipitation of carbides and the deformation without distinct shear lip might denote a significant reason, which leads to the degradation of unstable strain, compared with that at 0.001 s^{-1} and 25°C. Furthermore, the difference of fracture surfaces between tensile impact and quasi-static specimens reveals different deformation and fracture mechanisms corresponding to each loading condition. Its mechanism needs to be investigated further.

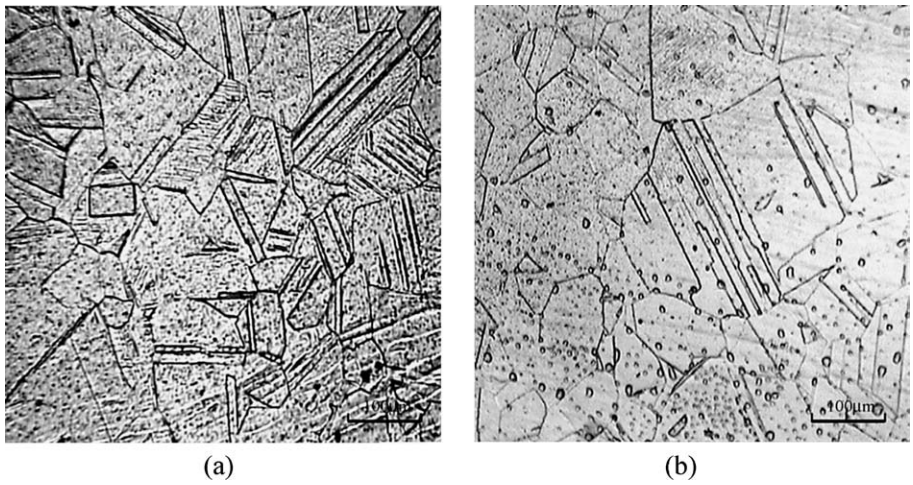

Figure 11 Macrostructure of the broken specimens tested at $\dot{\varepsilon} = 1200\ s^{-1}$ and different temperatures: (a) 25°C and (b) 537°C.

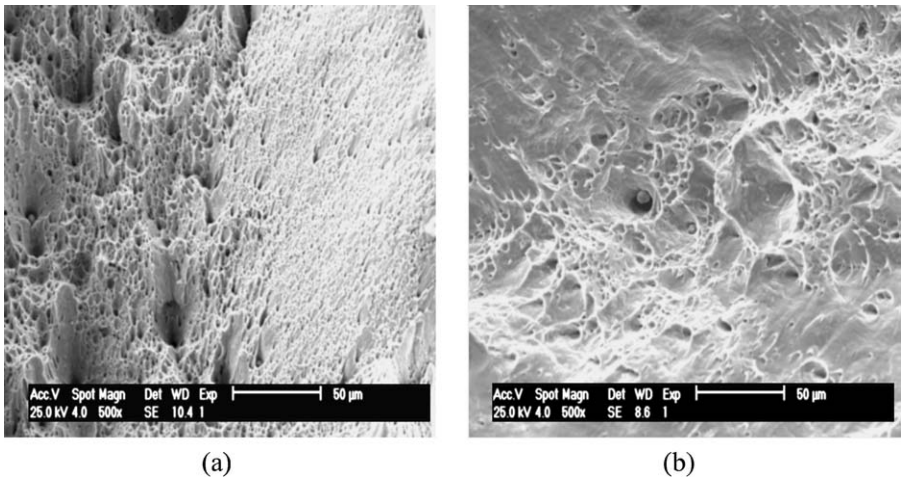

Figure 12 Tensile fractograph (SEM) of SUS304 at strain rate 0.001 s^{-1} and different temperatures: (a) 25°C and (b) 400°C.

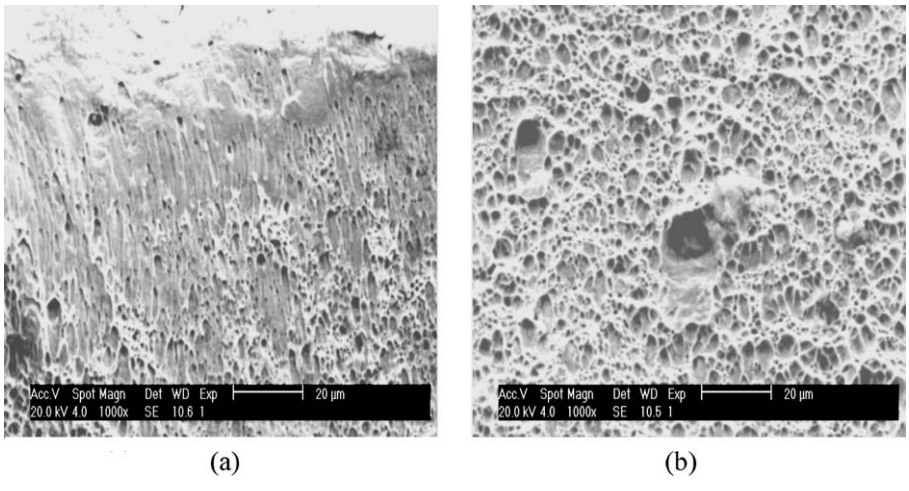

Figure 13 Tensile fractograph (SEM) of SUS304 at strain rate 1200 s^{-1} and 25°C: (a) egg-shaped dimples and (b) uniaxial dimples.

The volume fractions of transformation to martensite near the fracture surface are shown in Fig. 14. It can be seen that the austenite in SUS304 is metastable. The deformation-induced martensite transformation is correlated with the environment temperature in the quasi-static tests. The volume fraction of transformation to martensite decreases with the increasing temperature, which is consistent with the results reported in Ref. [30–32] and the elevated temperature embrittlement phenomenon at quasi-static loading. Based on the thermodynamics of martensite transformation, it is well known that the influence of temperature on $\gamma \rightarrow \alpha'$ transformation is both positive and negative. On one hand, with increasing temperature, the deformation is easily taking place due to the matrix softening, which promotes $\gamma \rightarrow \alpha'$ transformation. On the other hand, the austenite is more stable at higher temperatures and the critical stress of $\gamma \rightarrow \alpha'$ transformation increases as well [33]. Especially, when the temperature reaches or exceeds the sensitization temperature, the carbide deposition occurs in the γ crystal boundary. Such carbides restrain the plastic deformation of material so as to affect $\gamma \rightarrow \alpha'$ transformation. For SUS304 stainless steel, the latter plays predominant role in $\gamma \rightarrow \alpha'$ transformation. That is why the volume fraction of transformation to martensite in the present paper is lower at the same strain, compared with the results in Ref. [34]. Fig. 14 also shows a new phenomenon that the volume fraction of transformation to martensite is not sensitive to the environment temperature under high rate loading condition. The volume fraction of $\gamma \rightarrow \alpha'$ transformation under tensile impact at 25°C is approximately half of that under quasi-static tension at 25°C, which agrees with Ref. [34]. However, at elevated

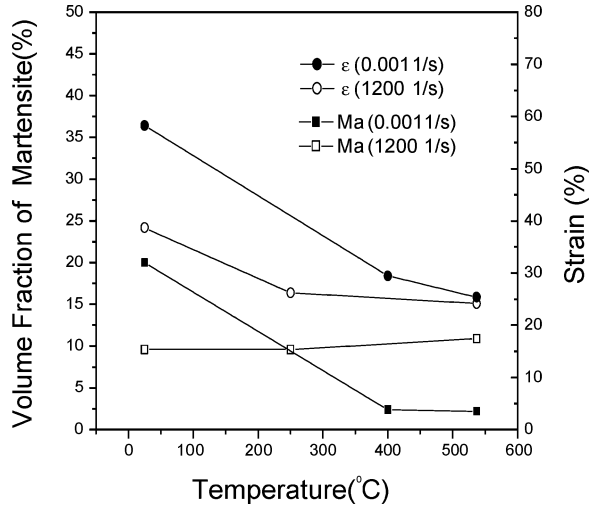

Figure 14 Volume fraction of martensite (Ma) and unstable strain (ε_b) vs. temperature at $\dot{\varepsilon} = 0.001\ s^{-1}$ and $\dot{\varepsilon} = 1200\ s^{-1}$.

temperatures, the volume fractions of $\gamma \rightarrow \alpha'$ transformation under tensile impact are several times to those under quasi-static loading. Such phenomenon reveals that the volume fraction of $\gamma \rightarrow \alpha'$ transformation depends not only on strain and temperature but also on strain rate. The mechanism needs to be investigated in the future.

4. Conclusion

1. An elevated temperature tensile impact experimental technique has been developed, using the rotating disk indirect bar-bar tensile impact apparatus with elevated temperature furnaces. Temperatures up to 800°C in the specimen have been obtained by means of rapid contact heating.

2. SUS304 stainless steel is a sort of temperature and strain-rate dependent metal, i.e., the strain rate has the effect of strengthening on yield stress and ultimate stress, but embrittling on unstable strain. The unstable strain decreases with increasing temperature at a constant strain rate, exhibiting elevated temperature embrittlement phenomenon.

3. The microstructure analysis reveals that the elevated temperature embrittlement phenomenon is due to the 'sensitization' of SUS304. In the case of impact loading, the adiabatic temperature rise is also capable of leading to sensitization. The differences of specimens' fractograph between tensile impact and quasi-static tension probably involve different deformation and fracture mechanisms.

4. The volume fraction of $\gamma \rightarrow \alpha'$ transformation depends on strain, temperature and strain rate. Its mechanism is worth discussing and investigating in the future.

Acknowledgement

The present work was supported by the National Natural Science Foundation of China (under contract No. 10172080). We are grateful to Dr. Xicheng Wei of the Shanghai University and Wen Huang and Heng Yi Wu of the University of Science and Technology of China for their help.

References

1. H. KOLSKY, *Proc. Phys. Soc. (London)* **B62** (1949) 676.
2. W. E. JAHNSMAN, *ASME J. Appl. Mech.* **Mar** (1971) 75.
3. J. Z. MALIONWAKI and J. R. KLEAPACZKO, *Int. J. Mech. Sci.* **28**(5) (1986) 381.
4. A. M. LENNON and K. T. RAMESH, *Intern. J. Plast.* **14**(12) (1998) 1279.
5. SIA NAMAT-NASSER, WEI-GUO GUO and DAVID P. KIHL, *J. Mech. Phys. Solid* **49** (2001) 1823.
6. J. HARDING, E. O. WOOD and J. D. CAMPBELL, *J. Mech. Eng. Sci.* **2** (1960) 88.
7. J. HARDING *et al.*, "Impact Testing of Fiber-Reinforced Composite Materials," in Proc. ICCM-IV, and Tokyo (1982) p. 845.
8. K. SAKA and J. HARDING, AD-A150619 (1984).
9. K. KAWATA, *Inst. Phys. Conf. Ser.* **47**(1) (1979) 71.
10. T. NICHOLAS, *Experim. Mech.* **21** (1981) 177.
11. G. H. STAAB and A. GILAT, **31** (1991) 232.
12. XIA YUANMING, WANG XIN and YANG BAOCHANG, *J. Mater. Sci. Lett.* **12** (1993) 1481.
13. Y. M. XIA, J. M. YUAN and B. C. YANG, *Comp. Sci. Tech.* **52** (1994) 499.
14. Z. WANG and Y. M. XIA, *Appl. Comp. Mater.* **3**(2) (1996) 89.
15. Z. WANG, Y. X. ZHOU and Y. M. XIA, *J. Mater. Sci.* **32**(9) (1997) 2387.
16. Y. M. XIA and Y. X. ZHOU, *Key Enging. Mater.* **177** (2000) 231.
17. Y. X. ZHOU and Y. M. XIA, *J. Mater. Sci.* **35**(4) (2000) 925.
18. *Idem.*, *Comp. Sci. Tech.* **60**(3) (2000) 403.
19. Y. WANG and Y. M. XIA, *ibid.* **60** (2000) 591.
20. W. HUANG, Y. WANG and Y. M. XIA, *J. Mater. Sci. Lett.* **21**(14) (2002) 1113.
21. D. C. BARTON, M. S. MIRZA, J. L. STURGES and M. WAHEED, *J. De Physique IV*, C8 **4**(Sept) (1994) 659.
22. J. HARDING and L. M. WELSH, *J. Mater. Sci.* **18** (1983) 1810.
23. G. H. STAAB, *Experim. Mech.* Sept. (1991) 232.
24. C. Y. WANG and Y. M. XIA, *Intern. J. Sol. Struct.* **37** (2000) 3305.
25. H. P. WAN, Y. WANG and Y. M. XIA, *Acta Mech. Sinica (in China, English Series)* **19**(2) (2003) 154.
26. SHIYING LU, TINGKAI ZHANG and CHANGQIANG YANG, in "Stainless Steel" (in Chinese) (The Atom Industry Publishing Company, China, 1995) p. 166.
27. YUANMING XIA, SHIGUO RAO and BAOCHANG YANG, *J. Experim. Mech.* **5**(2) (1990) 170 (in Chinese).
28. SIA NEMAT-NASSER, YEOU-FONG LI and JON B. ISAACE, *Mech. Mater.* **17** (1994) 111.
29. RAJEEV KAPOOR and SIA NEMAT-NASSER, *Mech. Mater.* **27** (1998) 1.
30. J. M. DIANI and D. M. PARKS, *J. Mech. Phys. Solid* **46**(9) (1998) 1613.
31. F. D. FISCHER, G. REISNER, E. WERNER, K. TANNAKA, G. CAILLETAUD and T. ANTRETTER, *Intern. J. Plast.* **16** (2000) 723.
32. WOEI-SHYAN and CHI-FENG LIN, *Script Mater.* **43** (2000) 777.
33. T. ATEL and M. COHEN, *Acta Metall.* **1** (1953) 531.
34. K. P. STAUDHAMMER, C. E. FRANTZ, S. S. HECKER and L. E. MURR, in "Shock Waves and High Strain Rate Phenomena in Metals—Concepts and Applications" (Plenum Press, 1981) p. 91.

Received 19 February 2003
and accepted 8 April 2004